

Giant proximity exchange and flat Chern band in 2D magnet-semiconductor heterostructures

Nisarga Paul, Yang Zhang, Liang Fu

Department of Physics, Massachusetts Institute of Technology, Cambridge, MA, USA

Van der Waals (vdW) heterostructures formed by two-dimensional magnets and semiconductors have provided a fertile ground for fundamental science and for spintronics. We present first-principles calculations finding a proximity exchange splitting of 14 meV equivalent to an effective Zeeman field of 120 T in the vdW magnet-semiconductor heterostructure $\text{MoS}_2/\text{CrBr}_3$, leading to a 2D spin-polarized half-metal with carrier densities ranging up to 10^{13} cm^{-2} . We consequently explore the effect of large exchange coupling on the electronic bandstructure when the magnetic layer hosts chiral spin textures such as skyrmions. A flat Chern band is found at a “magic” value of magnetization $\bar{m} \sim 0.2$ for Schrödinger electrons, and it generally occurs for Dirac electrons. The magnetic proximity induced anomalous Hall effect enables transport-based detection of chiral spin textures, and flat Chern bands provides an avenue for engineering various strongly correlated states.

Flat band materials have recently emerged as an area of intensive study in condensed matter physics [1–3]. Due to the dominance of many-body effects over the quenched kinetic energy, such systems provide avenues for realizing strongly correlated electronic states such as generalized Wigner crystals, magnetic orders, and superconductivity. At partially filling of a topological flat band, interaction effects can further lead to quantum anomalous Hall states [4–7] as proposed in twisted bilayer graphene (TBG) [8, 9] and transition metal dichalcogenide (TMD) moiré heterostructures [10–12]. A common element of moiré materials is the presence of a spatially varying periodic modulation, e.g. of interlayer tunneling strength, which generates narrow or flat minibands.

Such a modulation is also present in magnets hosting periodic spin textures, which couple to electrons as a Zeeman splitting with spatially varying orientation. Noncoplanar or chiral spin textures, including skyrmions and canted spirals or vortices, are characterized by their nonzero spin chirality defined as $\vec{S}_i \cdot (\vec{S}_j \times \vec{S}_k)$. Chiral spin textures have been the focus of recent interest due to the observation of skyrmions in a host of compounds and a large anomalous Hall effect in noncoplanar magnets [13–19]. Electrons coupled to skyrmions experience an emergent magnetic field which manifests in the topological Hall effect [20, 21]. The presence of electron minibands due to a superlattice modulation is common to both structural moirés and periodic spin textures [22–25], but the close analogy between the two types of systems has not yet been explored.

A natural question is whether chiral spin textures can provide a route to realizing *flat* bands. Indeed, the spatial profile of spin textures can be tuned by externally controllable parameters, such as magnetization and period, which may function similarly to twist angle or lattice mismatch in TBG or TMDs in optimizing band flatness. Moreover, the emergent magnetic field may generate mini-bands with Chern number [26], furthering the analogy with structural moirés. A possible hurdle is that the exchange coupling between localized spins and itin-

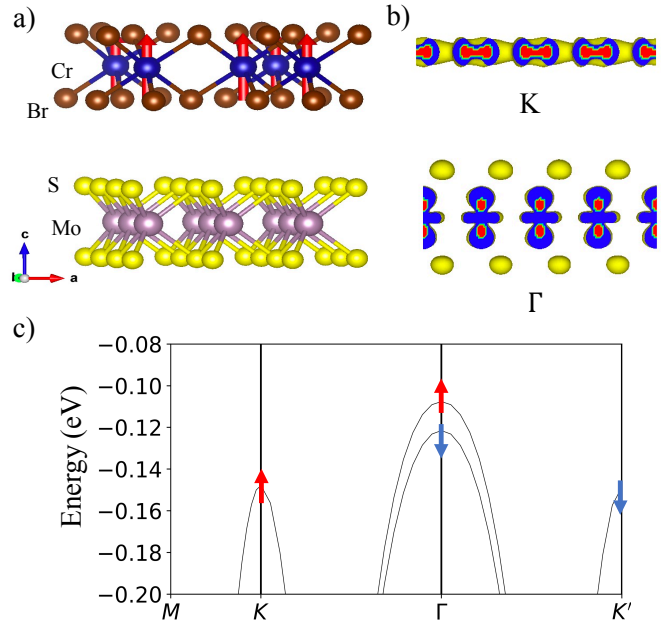


FIG. 1. (a) Lattice structure and magnetic order of $\text{MoS}_2/\text{CrBr}_3$ heterostructures. (b) Kohn-Sham wavefunction for K valley and Γ valley maximum. The K valley wavefunction is localized in the Mo layer, while the Γ valley wavefunction is spread out in the z direction. (c) Band structure of the fully relaxed $\text{MoS}_2/\text{CrBr}_3$ heterostructure with a 0.9 meV valley splitting at K'/K and 14 meV spin splitting at Γ .

erant electrons must be large for emergent field to have a strong effect on the electronic band structure. In reality, however, most skyrmion materials are high density metals in which the exchange splitting is small compared to the Fermi energy.

In this work, we propose a new platform for a topological flat band in 2D magnet/ TMD semiconductor heterostructures, in which the magnetic exchange coupling introduces an emergent Zeeman field acting on a low density of carriers in the semiconductor. Our study is motivated by the recent theoretical [27–30] and exper-

imental works [31] suggesting the existence of skyrmion phases and periodic chiral spin textures arising from a spatially varying interlayer coupling in magnetic moirés such as twisted bilayers of CrI_3 or CrBr_3 . Our two main results are as follows. First, we predict from first-principles calculations a giant exchange splitting of 14 meV in $\text{MoS}_2/\text{CrBr}_3$, which far exceeds the values found so far in 2D TMD/magnet heterostructures. As a result of this large exchange splitting, for a wide range of hole densities up to $0.83 \times 10^{13} \text{ cm}^{-2}$ only one spin-polarized band is occupied, leading to a 2D half metal. Second, we use a continuum model approach to study the effect of the emergent field from magnetic skyrmion crystals on the low-energy electronic structure of proximitized 2D semiconductors. We find an almost completely flat Chern band for Schrödinger electrons (as in MoS_2) at a “magic” value of magnetization $\bar{m} = 0.2$, while for Dirac electrons (as in graphene), remarkably, a flat Chern band always occurs.

Giant exchange splitting in $\text{MoS}_2/\text{CrBr}_3$.— Our proposal to realize flat Chern bands requires a strong interfacial exchange coupling in 2D magnet-TMD semiconductor heterostructures. In monolayer TMDs, strong Ising spin-orbit coupling and inversion symmetry breaking gives rise to opposite spin states in the K' and K valleys. Previous studies have demonstrated K'/K spin-valley splitting in TMDs proximity coupled to ferromagnetic semiconductors. However, such splitting is generally small, e.g., 3.5 meV in $\text{WSe}_2/\text{CrI}_3$ [32].

We performed density functional calculations using the generalized gradient approximation [33] with SCAN+rVV10 van der Waals density functional [34], as implemented in the Vienna Ab initio Simulation Package [35]. By scanning through various 2D TMD-magnet heterostructures, we find a giant exchange splitting in $\text{MoS}_2/\text{CrBr}_3$, where monolayer MoS_2 is a TMD semiconductor, and CrBr_3 is an insulating vdW magnet. Magnetic orders and lattice constants are taken from the Computational 2D Materials Database (C2DB) [36]. The 2x2 supercell of MoS_2 with lattice constant 6.38 Å is chosen to match the lattice constant of CrBr_3 (6.44 Å) with less than 1% strain. Similar to previous works, we find a small K'/K valley splitting on the valence band side of 0.9 meV for $\text{MoS}_2/\text{CrBr}_3$.

In monolayer MoS_2 , the Γ valley is very close in energy to the K valley. In $\text{MoS}_2/\text{CrBr}_3$, we find that the Γ valley of MoS_2 becomes the valence band maximum after taking into account the relaxed heterostructure with layer spacing 6.76 Å. We observe a giant spin splitting of up to 14 meV in the Γ valley as shown in Fig. 1. Assuming a Landé g -factor equal to 2, this is an effective Zeeman field of 120 T. The large difference in the exchange splitting in the K and Γ valleys can be understood from the spatial distribution of wavefunctions. At the K valley, due to the large in-plane momentum, electron wavefunctions are strongly localized within the vdW layer. However,

at the Γ valley, due to the zero in-plane momentum, the wavefunctions are more spread out in out-of-plane direction, which enhances coupling to the magnetic layer. The large exchange splitting in this specific material, which is the first main result of this work, provides efficient spin control of the Γ valley bands.

Emergent gauge field at large exchange coupling.— In the following, we explore the consequences of a large exchange coupling on the electronic bandstructure. This is motivated by both the giant exchange splitting found in the previous section and theoretical and experimental results suggesting that twisted bilayers of vdW magnets may host noncoplanar or skyrmionic phases [27–31]. To this end, we turn to a completely general Hamiltonian describing electrons coupled to a spin texture via a large exchange coupling. It is important to note that in low density systems such as TMD semiconductors or graphene, the physics of itinerant electrons coupled to periodic spin textures is universally described by a continuum theory, taking the form

$$H_S = \frac{p^2}{2m} + J\vec{\sigma} \cdot \vec{S}(r) \quad (1a)$$

$$H_D = v\vec{p} \cdot \vec{\tau} + J\vec{\sigma} \cdot \vec{S}(r) \quad (1b)$$

for the case of Schrödinger and Dirac electrons with mass m and velocity v , respectively. The Pauli $\vec{\sigma}$ matrices act on electron spin, while the Pauli $\vec{\tau}$ matrices act on a pseudospin degree of freedom, e.g., sublattice in the case of graphene. In the following, we will consider smoothly varying periodic spin textures $\vec{S}(r)$ with magnetic wavelength ξ and unit norm $|\vec{S}| = 1$. An SU(2) gauge transformation $\mathbf{U}(r)$ allows us to instead consider a uniformly polarized spin texture provided we use the gauge-transformed momentum $\vec{p} - e\vec{\mathbf{A}}$, where

$$\vec{\mathbf{A}} = \frac{i\hbar}{e} \mathbf{U}^\dagger \vec{\nabla} \mathbf{U}. \quad (2)$$

The large exchange coupling limits are, respectively,

$$Jm\xi^2 \gg 1 \quad \text{and} \quad J\xi/v \gg 1. \quad (3)$$

In this limit the ground state manifold consists of electrons with spins locally anti-aligned with the spin texture. The effective Hamiltonian describing the locally spin-polarized Schrödinger electrons has been derived before [20]:

$$\tilde{H}_S = \frac{1}{2m}(\vec{p} - e\vec{\mathbf{A}})^2 + \frac{e^2}{8m}(\partial_i \vec{S})^2 \quad (4)$$

(summing $i = x, y$). The second term, originating from off-diagonal terms of $\vec{\mathbf{A}}$, is a scalar potential that accounts for the reduction of electron hopping by the spin

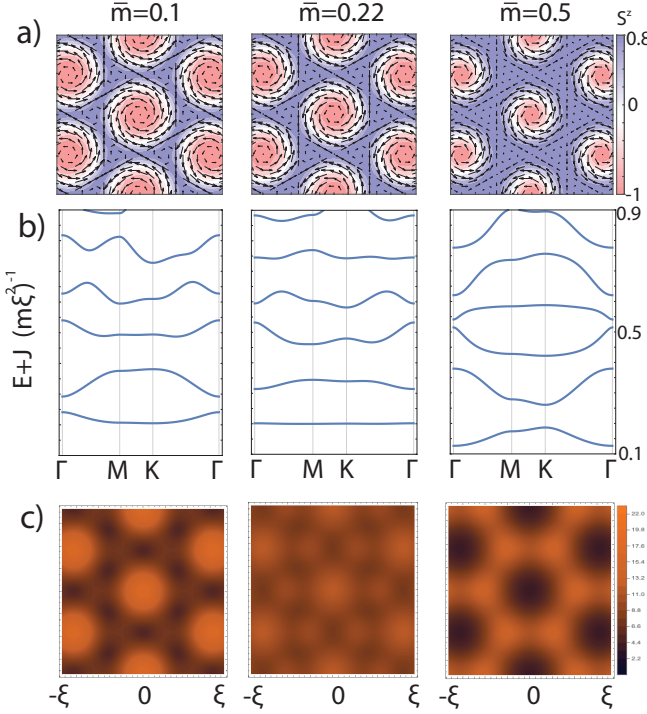


FIG. 2. (a) Skyrmion texture based on generic ansatz Eq. (7) with different magnetizations and $\alpha = 1$. (S^x, S^y) is plotted as a vector field with S^z in color, and \bar{m} is the average of S^z . (b) Bandstructures in the presence of the textures in (a), following the $\Gamma M K \Gamma$ path in the hexagonal mini BZ. H_S was diagonalized using a plane-wave cutoff $N = 10$, taking $J = 100, m = 1$. A flat first band is observed when $\bar{m} = 0.22$. All bands carry Chern number $C = 1$. (c) Local density of states summed over the first band (sampling 4^2 states), spatially aligned with (a).

gradient and $\vec{A} = [\vec{A}]_{\downarrow\downarrow}$ is an emergent $U(1)$ gauge field. The corresponding emergent field strength

$$B^e = \frac{\hbar}{2e} \vec{S} \cdot (\partial_x \vec{S} \times \partial_y \vec{S}) \quad (5)$$

is proportional to the spin chirality. A skyrmion can be defined as a texture with flux h/e . It follows from this equation that purely in-plane spin textures have vanishing emergent field. Moreover, purely in-plane textures are symmetric under the combination of time reversal and a spin-space C_2 rotation, while the Chern number is odd under this combination, implying such textures do not yield topological bands. Accordingly, we will consider chiral magnets with out-of-plane spin textures.

We will also be interested in Dirac electrons at large exchange coupling, for which the effective Hamiltonian takes the form

$$\tilde{H}_D = v(\vec{p} - e\vec{A}) \cdot \vec{\tau}. \quad (6)$$

It is notable that Dirac electrons only feel a periodic gauge field in contrast with the previously studied

Schrödinger case involving both the gauge field and a scalar potential.

The origin of the emergent gauge field is the local $U(1)$ rotational freedom of the electron spin about the axis of the local spin. In analogy with conventional Landau levels, the emergent field B^e generally endows the minibands with Chern number when the average is nonzero. In the following, we investigate the flatness of the induced Chern bands in the large exchange coupling limit.

Flat bands in skyrmion crystals.— We present numerical results on the bandstructure of Schrödinger and Dirac electrons in the presence of generic skyrmion crystals using the full Hamiltonians in Eqs. (1a) and (1b), i.e. without any approximations. H_S and H_D are explicitly diagonalized in a plane wave basis with a large wavenumber cutoff N (see Supplemental Material).

As a model for a generic SkX, we introduce the simple three-parameter ansatz $\vec{S} = \vec{N}_r / |\vec{N}_r|$ with

$$\vec{N}_r = \frac{1}{\sqrt{2}} \sum_{j=1}^6 e^{iq_j \cdot \vec{r}} \hat{e}_j + \mu \hat{z} \quad (7)$$

where $\vec{q}_j = (\xi(\cos \theta_j, \sin \theta_j))$ and $\hat{e}_j = (i\alpha \sin \theta_j, -i\alpha \cos \theta_j, -1)/\sqrt{2}$ and the angles satisfy $\theta_2 = \theta_1 + 2\pi/3, \theta_3 = \theta_1 + 4\pi/3$, and $\theta_{j+3} = \theta_j + \pi$. Eq. (7) represents a normalized sum of three helical spirals forming a triangular SkX, as plotted in Fig. 2a. This ansatz is widely adopted in studies of chiral magnets and magnetic skyrmion crystals. It qualitatively reproduces the observed real-space images of skyrmion crystals [37–43]. A different choice of relative phases results in Néel-like skyrmions but doesn't alter bandstructures. The parameters α, ξ , and μ control coplanarity, wavelength, and out-of-plane bias, respectively.

In Fig. 2 we plot bandstructures and local density of states (LDOS) for Schrödinger electrons in the presence of our chosen SkX. We set $\alpha = 1$ and vary the magnetization \bar{m} (i.e. the unit cell average of S^z), which is monotonic with μ (ξ can be scaled out of the problem). We can observe the flattening of lower bands and a near perfectly flat, well-separated first band as we tune the magnetization past $\bar{m} = 0.2$, the second main result of this work. All bands shown carry Chern number $C = 1$ and spins are anti-aligned with the skyrmion texture.

In Fig. 3 we systematically plot band flatness, defined as the ratio of bandwidth to bandgap for the first miniband, with varying α and \bar{m} . Complete flatness is an ideal pathway for strongly correlated matter since the kinetic energy is strongly quenched and band separation remains large. We plot the branch $\bar{m} > 0$ which corresponds to the typical case of separated skyrmion bubbles. The plot indicates a quite robust “magic” value of magnetization near $\bar{m} = 0.2$ where flatness goes to zero.

Next we turn to the case of Dirac electrons under periodic Zeeman field, which may be realized in graphene

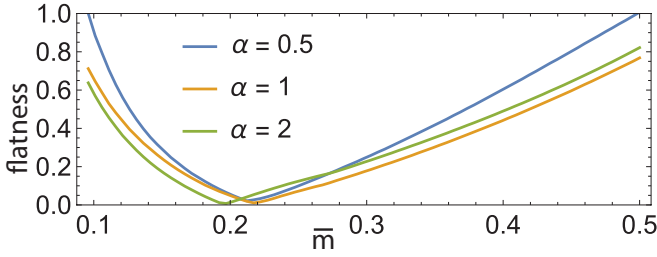


FIG. 3. First band flatness, defined as the ratio of bandwidth to bandgap, of H_S in the presence of a generic skyrmion crystal (defined in Eq. (7)) with varying magnetization \bar{m} and coplanarity α . Near perfect flatness occurs around $\bar{m} = 0.2$. Flatness was calculated by solving H_S with plane-wave cutoff $N = 10$ and $J = 100$ over 10^2 points in the mini BZ.

or twisted bilayer graphene in proximity with a 2D magnet. Remarkably, we observe a flat band for *arbitrary* skyrmion textures in Fig. 4. This can be understood from the effective Hamiltonian in the large J limit.

$$\tilde{H}_D = v \begin{pmatrix} 0 & \Pi \\ \bar{\Pi} & 0 \end{pmatrix} \quad (8)$$

where $\bar{\Pi} = (\Pi_x + i\Pi_y)/2$ and $\vec{\Pi} = \vec{p} - e\vec{A}$. It is known that the Dirac equation in the presence of a spatially varying magnetic field admits an extensive set of zero-mode solutions [44]. The number of zero modes is equal to the total number of flux quanta through the system (which in our case is given by the total topological charge of the skyrmion crystal), regardless of the spatial profile of the magnetic field. This remarkable property follows from the Atiyah-Singer index theorem. In the limit of a uniform field, these zero modes reduce to the well-known $n = 0$ Landau level.

In Fig. 4a we plot the periodic emergent magnetic fields arising from the skyrmion crystal and in Fig. 4c we plot the LDOS of the flat band of Dirac electrons under magnetic proximity effect. The LDOS shows significant spatial variation, which can be detected by scanning tunneling microscopy.

Small exchange coupling and anomalous Hall effect.— While the large exchange coupling regime is realistic for $\text{MoS}_2/\text{CrBr}_3$, other systems may have constraints on magnetic wavelength or intrinsic exchange coupling not conducive to this limit. Additionally, many chiral magnets host noncoplanar states which do not enclose a net spin chirality. Examples of such states include the canted vortex lattice, multiple-Q conical spiral, multilayers of single-Q helices, and meron-antimeron lattice [29, 30].

Remarkably, we find that neither net spin chirality nor large exchange coupling is necessary to attain Chern bands and even generic noncoplanar textures may generate an anomalous Hall effect at small coupling. This goes beyond the mean-field semiclassical result [20] that the

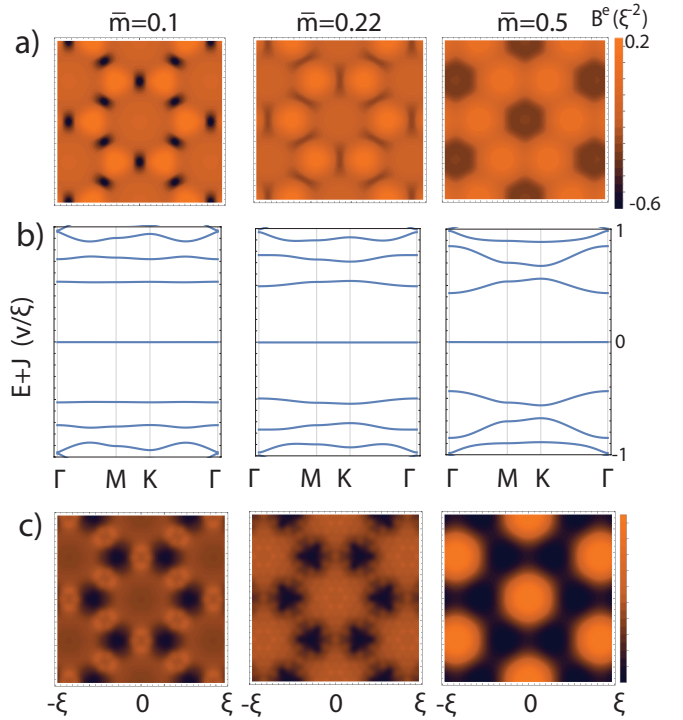


FIG. 4. (a) Emergent magnetic fields corresponding to (and spatially aligned with) the SkX shown in Fig. 2a. Dirac electrons in the large exchange coupling limit move in this emergent field. (b) Bandstructures analogous to Fig. 2b for Dirac electrons. A flat band is pinned at $E = -J$ whenever there is net emergent flux. (c) Local density of states summed over the $E = -J$ band (sampling 150 states), spatially aligned with (a).

anomalous Hall effect in topological textures is proportional to the net spin chirality. We provide examples of spin textures illustrating this point in the Supplemental Material. The observation of marked Hall transport features suggests that proximity-coupled electrons can serve as a reliable sensor for noncoplanar textures in magnetic materials (Fig. 5). A transport-based sensor would be advantageous because it can be done on tabletop while bulk probes such as Lorentz TEM and neutron diffraction have a low sensitivity for 2D devices. We also note that in the presence of a point-group symmetry, the leading Fourier modes of the a spin texture may be inferred from the miniband Chern numbers. This provides a useful direct mapping between real-space textures and transport properties. In the Supplemental Material, we present the details for the case of six-fold rotational symmetry.

Conclusions.— We investigated the emergence of flat bands in semiconductors proximity-coupled to spin textures in the limit of large exchange coupling. This limit was motivated by the giant exchange of 14 meV we found using first-principles calculations in the TMD/vdW magnet heterostructure $\text{MoS}_2/\text{CrBr}_3$, the latter of which is proposed to host skyrmions in a moiré [27, 28]. For

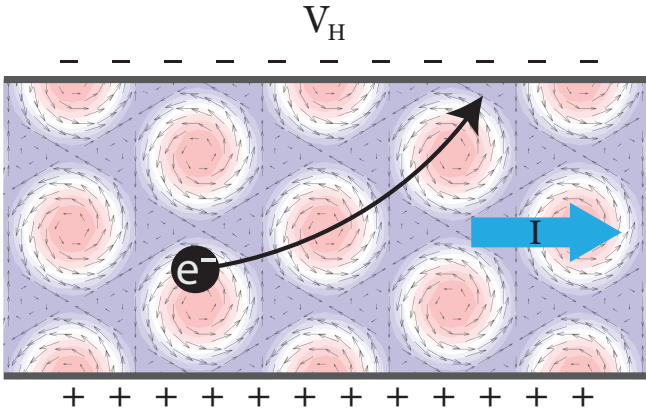


FIG. 5. An anomalous Hall effect is generically expected in semiconductor / chiral magnet heterostructures with non-coplanar textures even at small coupling and without net spin chirality.

Schrödinger electrons coupled to a generic SkX we find a flat Chern band emerges at out-of-plane magnetization $\bar{m} = 0.2$ while a flat Chern band is generically present for Dirac electrons. A large exchange coupling and long electron mean free path (for sharply defined minibands) are prerequisites for this route to flat bands. These continuum results are universal at low densities, only making use of effective mass or Dirac velocity in the band structure. We show explicitly that anomalous Hall effect is generically present in TMD semiconductors or graphene proximitized by noncoplanar magnets. Our results also suggest the possibility of fractional Chern insulators (FCIs) in 2D magnet-semiconductor or graphene heterostructures.

Acknowledgements— We thank Joe Checkelsky, Takashi Kurumaji, Kin Fai Mak, Jie Shan, Riccardo Comin and Xiaodong Xu for helpful discussions, and Junkai Dong for collaboration on a related project. This work is funded by the Simons Foundation through a Simons Investigator Award. LF is partly supported by the David and Lucile Packard Foundation.

- [1] E. Y. Andrei and A. H. MacDonald, Graphene bilayers with a twist, *Nat. Mater.* **19**, 1265 (2020).
- [2] T. T. Heikkilä, N. B. Kopnin, and G. E. Volovik, Flat bands in topological media, *JETP Lett.* **94**, 233 (2011).
- [3] E. Tang and L. Fu, Strain-induced partially flat band, helical snake states and interface superconductivity in topological crystalline insulators, *Nat. Phys.* **10**, 964 (2014).
- [4] M. Serlin, C. L. Tschirhart, H. Polshyn, Y. Zhang, J. Zhu, K. Watanabe, T. Taniguchi, L. Balents, and A. F. Young, Intrinsic quantized anomalous hall effect in a moire heterostructure, *Science* **367**, 900 (2020).
- [5] A. L. Sharpe, E. J. Fox, A. W. Barnard, J. Finney, K. Watanabe, T. Taniguchi, M. A. Kastner, and

- D. Goldhaber-Gordon, Emergent ferromagnetism near three-quarters filling in twisted bilayer graphene, *Science* **365**, 605 (2019).
- [6] G. Chen, A. L. Sharpe, E. J. Fox, Y.-H. Zhang, S. Wang, L. Jiang, B. Lyu, H. Li, K. Watanabe, T. Taniguchi, Z. Shi, T. Senthil, D. Goldhaber-Gordon, Y. Zhang, and F. Wang, Tunable correlated chern insulator and ferromagnetism in a moire superlattice, *Nature* **579**, 56 (2020).
- [7] T. Li, S. Jiang, B. Shen, Y. Zhang, L. Li, T. Devakul, K. Watanabe, T. Taniguchi, L. Fu, J. Shan, and K. F. Mak, Quantum anomalous Hall effect from intertwined moire bands, *arXiv* (2021), 2107.01796.
- [8] Y.-H. Zhang, D. Mao, and T. Senthil, Twisted bilayer graphene aligned with hexagonal boron nitride: Anomalous hall effect and a lattice model, *Phys. Rev. Research* **1**, 033126 (2019).
- [9] M. Xie and A. H. MacDonald, Nature of the correlated insulator states in twisted bilayer graphene, *Phys. Rev. Lett.* **124**, 097601 (2020).
- [10] F. Wu, T. Lovorn, E. Tutuc, I. Martin, and A. H. MacDonald, Topological insulators in twisted transition metal dichalcogenide homobilayers, *Phys. Rev. Lett.* **122**, 086402 (2019).
- [11] T. Devakul, V. Crépel, Y. Zhang, and L. Fu, Magic in twisted transition metal dichalcogenide bilayers, *arXiv* (2021), 2106.11954 (Nature Communications— in the press).
- [12] Y. Zhang, T. Devakul, and L. Fu, Spin-textured Chern bands in AB-stacked transition metal dichalcogenide bilayers, *Proc. Natl. Acad. Sci. U.S.A.* **118**, e2112673118 (2021).
- [13] S. Mühlbauer, B. Binz, F. Jonietz, C. Pfleiderer, A. Rosch, A. Neubauer, R. Georgii, and P. Böni, Skyrmion lattice in a chiral magnet, *Science* **323**, 915 (2009).
- [14] X. Z. Yu, N. Kanazawa, W. Z. Zhang, T. Nagai, T. Hara, K. Kimoto, Y. Matsui, Y. Onose, and Y. Tokura, Skyrmion flow near room temperature in an ultralow current density, *Nature Communications* **3**, 988 (2012).
- [15] N. Nagaosa and Y. Tokura, Topological properties and dynamics of magnetic skyrmions, *Nature Nanotechnology* **8**, 899 (2013).
- [16] F. Büttner, I. Lemesh, and G. S. D. Beach, Theory of isolated magnetic skyrmions: From fundamentals to room temperature applications, *Scientific Reports* **8**, 283 (2018).
- [17] Y. Machida, S. Nakatsuji, S. Onoda, T. Tayama, and T. Sakakibara, Time-reversal symmetry breaking and spontaneous hall effect without magnetic dipole order, *Nature* **463**, 210 (2010).
- [18] S. Nakatsuji, N. Kiyohara, and T. Higo, Large anomalous hall effect in a non-collinear antiferromagnet at room temperature, *Nature* **527**, 212 (2015).
- [19] A. K. Nayak, J. E. Fischer, Y. Sun, B. Yan, J. Karel, A. C. Komarek, C. Shekhar, N. Kumar, W. Schnelle, J. Kübler, *et al.*, Large anomalous hall effect driven by a nonvanishing berry curvature in the noncollinear antiferromagnet mn₃ge, *Science advances* **2**, e1501870 (2016).
- [20] P. Bruno, V. K. Dugaev, and M. Taillefumier, Topological hall effect and berry phase in magnetic nanostructures, *Phys. Rev. Lett.* **93**, 096806 (2004).
- [21] A. Neubauer, C. Pfleiderer, B. Binz, A. Rosch, R. Ritz, P. G. Niklowitz, and P. Boni, Topological hall effect in

the a phase of mnsi, Phys. Rev. Lett. **102**, 186602 (2009).

[22] N. Paul and L. Fu, Topological magnetic textures in magnetic topological insulators, Phys. Rev. Res. **3**, 033173 (2021).

[23] C.-K. Li, X.-P. Yao, and G. Chen, Twisted magnetic topological insulators, Phys. Rev. Research **3**, 033156 (2021).

[24] S. Divic, H. Ling, T. Pereg-Barnea, and A. Paramekanti, Magnetic skyrmion crystal at a topological insulator surface, arXiv (2021), 2103.15841.

[25] G. Chen, M. Khosravian, J. L. Lado, and A. Ramires, Designing spin-textured flat bands in twisted graphene multilayers via helimagnet encapsulation, arXiv (2021), 2109.13130.

[26] K. Hamamoto, M. Ezawa, and N. Nagaosa, Quantized topological hall effect in skyrmion crystal, Phys. Rev. B **92**, 115417 (2015).

[27] Q. Tong, F. Liu, J. Xiao, and W. Yao, Skyrmions in the moiré of van der waals 2d magnets, Nano Lett. **18**, 7194 (2018).

[28] K. Hejazi, Z.-X. Luo, and L. Balents, Noncollinear phases in moiré magnets, Proc. Natl. Acad. Sci. U.S.A. **117**, 10721 (2020).

[29] X. Lu, R. Fei, L. Zhu, and L. Yang, Meron-like topological spin defects in monolayer crcl3, Nat. Commun. **11**, 1 (2020).

[30] M. Augustin, S. Jenkins, R. F. L. Evans, K. S. Novoselov, and E. J. G. Santos, Properties and dynamics of meron topological spin textures in the two-dimensional magnet crcl3, Nat. Commun. **12**, 1 (2021).

[31] Y. Xu, A. Ray, Y.-T. Shao, S. Jiang, D. Weber, J. E. Goldberger, K. Watanabe, T. Taniguchi, D. A. Muller, K. F. Mak, and J. Shan, Emergence of a noncollinear magnetic state in twisted bilayer CrI3, arXiv (2021), 2103.09850.

[32] D. Zhong, K. L. Seyler, X. Linpeng, R. Cheng, N. Sivadas, B. Huang, E. Schmidgall, T. Taniguchi, K. Watanabe, M. A. McGuire, *et al.*, Van der waals engineering of ferromagnetic semiconductor heterostructures for spin and valleytronics, Science advances **3**, e1603113 (2017).

[33] J. P. Perdew, K. Burke, and M. Ernzerhof, Generalized gradient approximation made simple, Physical review letters **77**, 3865 (1996).

[34] H. Peng, Z.-H. Yang, J. P. Perdew, and J. Sun, Versatile van der waals density functional based on a meta-generalized gradient approximation, Physical Review X **6**, 041005 (2016).

[35] G. Kresse and J. Furthmüller, Efficiency of ab-initio total energy calculations for metals and semiconductors using a plane-wave basis set, Computational materials science **6**, 15 (1996).

[36] S. Haastrup, M. Strange, M. Pandey, T. Deilmann, P. S. Schmidt, N. F. Hinsche, M. N. Gjerding, D. Torelli, P. M. Larsen, A. C. Riis-Jensen, *et al.*, The computational 2d materials database: high-throughput modeling and discovery of atomically thin crystals, 2D Materials **5**, 042002 (2018).

[37] K. Karube, J. S. White, D. Morikawa, M. Bartkowiak, A. Kikkawa, Y. Tokunaga, T. Arima, H. M. Rønnow, Y. Tokura, and Y. Taguchi, Skyrmion formation in a bulk chiral magnet at zero magnetic field and above room temperature, Phys. Rev. Mater. **1**, 074405 (2017).

[38] J.-H. Park and J. H. Han, Zero-temperature phases for chiral magnets in three dimensions, Phys. Rev. B **83**, 184406 (2011).

[39] Y. Tokura and N. Kanazawa, Magnetic Skyrmion Materials, Chem. Rev. 10.1021/acs.chemrev.0c00297 (2020).

[40] S.-Z. Lin and S. Hayami, Ginzburg-landau theory for skyrmions in inversion-symmetric magnets with competing interactions, Phys. Rev. B **93**, 064430 (2016).

[41] K. Shimizu, S. Okumura, Y. Kato, and Y. Motome, Spin moire engineering of topological magnetism and emergent electromagnetic fields, Phys. Rev. B **103**, 184421 (2021).

[42] X. Z. Yu, Y. Onose, N. Kanazawa, J. H. Park, J. H. Han, Y. Matsui, N. Nagaosa, and Y. Tokura, Real-space observation of a two-dimensional skyrmion crystal, Nature **465**, 901 (2010).

[43] A. Tonomura, X. Yu, K. Yanagisawa, T. Matsuda, Y. Onose, N. Kanazawa, H. S. Park, and Y. Tokura, Real-space observation of skyrmion lattice in helimagnet mnsi thin samples, Nano Lett. **12**, 1673 (2012).

[44] Y. Aharonov and A. Casher, Ground state of a spin-1/2 charged particle in a two-dimensional magnetic field, Phys. Rev. A **19**, 2461 (1979).

[45] C. Fang, M. J. Gilbert, and B. A. Bernevig, Bulk topological invariants in noninteracting point group symmetric insulators, Phys. Rev. B **86**, 115112 (2012).

Supplemental Material

Bandstructure

We present the separate band structures of 2×2 MoS₂ and CrBr₃ in Fig. 6. The K valley is 30 meV higher than the Γ valley in monolayer MoS₂. Due to the type II band alignment, the band gap of the heterobilayer is reduced to 1.2 eV.

The plane wave approximation for the continuum model is as follows. Let $\vec{S}(r) = \vec{S}(r+a_1) = \vec{S}(r+a_2)$ be a doubly periodic spin texture and let b_1, b_2 be the reciprocal vectors, $b_i \cdot a_j = 2\pi\delta_{ij}$. We can write any wavefunction with momentum $k = (k_x, k_y)$ as

$$\psi(r) = e^{ikr} \sum_{m_1, m_2} e^{i(m_1 b_1 + m_2 b_2) r} \chi_{m_1 m_2} \quad (9)$$

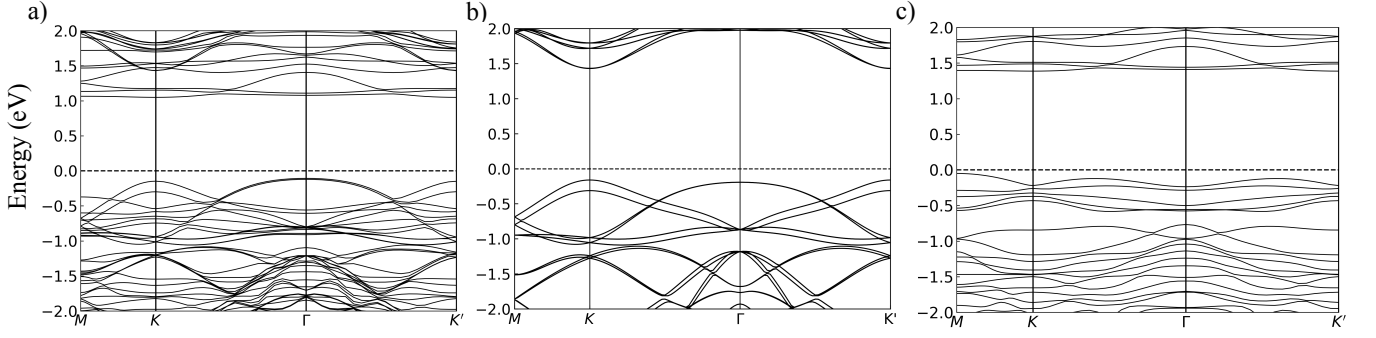


FIG. 6. Band structure of (a) MoS₂/CrBr₃, (b) 2 × 2 MoS₂, (c) CrBr₃.

where m_1, m_2 are integers and $\chi_{m_1 m_2} = \begin{pmatrix} \chi_{m_1 m_2}^\uparrow \\ \chi_{m_1 m_2}^\downarrow \end{pmatrix}$. The Hamiltonian can be written as

$$H_S = \frac{p^2}{2m} \mathbf{1} + J \sum_{m_1, m_2} e^{i(m_1 b_1 + m_2 b_2) r} \vec{S}_{m_1 m_2} \cdot \vec{\sigma} \quad (10)$$

where $\vec{S}_{m_1 m_2} = \vec{S}_{-m_1, -m_2}^*$ is a Fourier component of $\vec{S}(r)$. We then obtain the matrix equation

$$\frac{(k + n_1 b_1 + n_2 b_2)^2}{2m} \chi_{n_1 n_2} + J \sum_{m_1 m_2} \vec{S}_{m_1 m_2} \cdot \vec{\sigma} \chi_{n_1 - m_1, n_2 - m_2} = E \chi_{n_1 n_2} \quad (11)$$

We apply a large momentum cutoff $|n_1|, |n_2| \leq N$ to approximate the spectrum and eigenfunctions, with an analogous procedure for the Dirac case. In the Dirac case we omit spurious modes which appear on the lattice edges and whose support is measure zero as $N \rightarrow \infty$, which can be easily identified as they break the C_6 symmetry. The plane wave method was used for Fig.s 1, 3, and 4 while for Fig. 7 a square lattice nearest neighbor tight-binding Hamiltonian was used.

Small exchange coupling and anomalous Hall effect

In the large exchange coupling regime, we found well-separated flat Chern bands (which imply a quantized anomalous Hall effect) in the presence of skyrmion-like textures. If we drop these two prerequisites and instead consider small exchange coupling and general noncoplanar textures (i.e. not necessarily enclosing a net spin chirality), we find numerically that an anomalous Hall conductance is still generically present. We illustrate this point with an SkX at small exchange coupling (Fig. 7a) and a canted vortex lattice spin texture, which takes the form

$$\vec{S}_r = (\sqrt{1 - (S^z)^2} \sin \theta_r, \sqrt{1 - (S^z)^2} \cos \theta_r, S^z) \quad (12)$$

with θ_r the angle relative to the unit cell center and S^z is a smooth periodic function which equals unity at the unit cell centers. We chose $S^z(r) = \frac{1}{3} \sum_i \cos^2(q_i \cdot r/2)$ where $q_1 = b_1, q_2 = b_2, q_3 = -b_1 - b_2$ and $b_{1,2}$ are reciprocal lattice vectors. This texture has alternating regions of $\pm 1/2$ emergent flux, so it may also be considered to be a meron-antimeron lattice. Because the net spin chirality vanishes, and naïvely we may expect no momentum-space topology. However, we observe miniband Chern numbers and a corresponding anomalous Hall effect (Fig. 7b).

In the following, we connect the leading Fourier modes of point-group symmetric spin textures to the Chern number of associated electron bands. We approach this by using perturbation theory in a small exchange coupling J , in which case Chern numbers can be computed from the point-group symmetry eigenvalues of the states at the high-symmetry points in the Brillouin zone [45]. These eigenvalues in turn depend only on the leading Fourier modes of the spin texture. We assume a six-fold rotational symmetry of the Hamiltonian, i.e. $[\hat{C}_6, H] = 0$ where $\hat{C}_6 = e^{-\frac{2\pi i}{6} L^z} e^{-\frac{2\pi i}{6} \frac{\sigma^z}{2}}$ (other point-groups can be analyzed similarly). The Chern number C is given by

$$e^{2\pi i C/6} = \prod_{i \in \text{occ.}} (-1)^F \eta_i(\Gamma) \theta_i(K) \zeta_i(M) \quad (13)$$

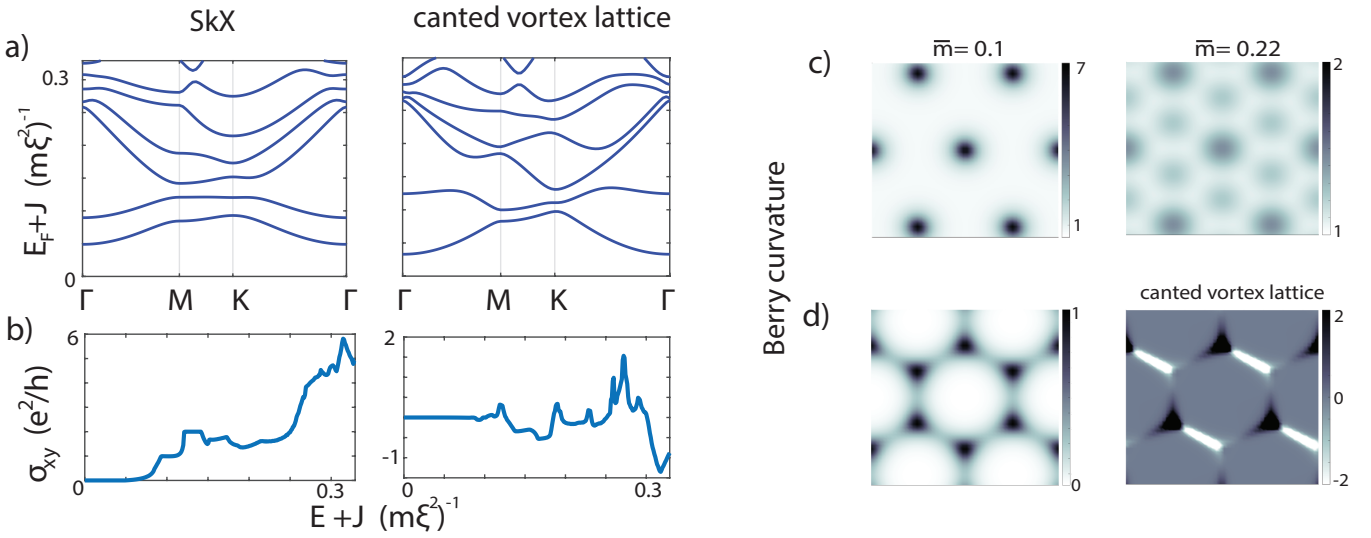


FIG. 7. (a) Weak-coupling bandstructures for the SkX ($\bar{m} = 0.1, \alpha = 1$) and the canted vortex lattice (or meron-antimeron lattice). Each band in the former has Chern number 1, and the lowest bands in the latter have Chern numbers [0,0,1,-1,1]. (b) Hall conductances. The SkX exhibits a quantized anomalous Hall effect from the lowest bands, and the canted vortex lattice has a nonzero anomalous Hall response despite its vanishing net spin chirality. (c) Rescaled Berry curvature $|b_1|^2\Omega(\mathbf{k})/2\pi$ corresponding to the lowest bands in in Fig. 2b plotted in a square of size $2|b_1|$. Berry curvature becomes more uniform near the flat band at $\bar{m} = 0.22$. (d) Similarly for an SkX (left) and canted vortex lattice (right) at weak exchange coupling, corresponding to the lowest bands of (a)

where $\eta(\Gamma)$ is the C_6 eigenvalue at the Γ point, $\theta(K)$ is the C_3 eigenvalue at the K point, and $\zeta(M)$ is the C_2 eigenvalue at the M point. The Chern number for the first band follows from degenerate perturbation theory, and we obtain

$$C \bmod 6 = \begin{cases} 1 & S_0^z > 0, S_1^z > 0 \\ 2 \text{ or } 0 & S_0^z > 0, S_1^z < 0 \\ -2 \text{ or } 0 & S_0^z < 0, S_1^z > 0 \\ -1 & S_0^z < 0, S_1^z < 0 \end{cases} \quad (14)$$

assuming $J > 0$. For $J < 0$ the Chern number changes sign mod 6. Here \vec{S}_0, \vec{S}_1 are the zeroth and first Fourier components of $\vec{S}(r)$, so in particular $S_0^z = \bar{m}$. For fixed S_1^z , we may note that the first band undergoes a topological transition as the magnetization changes sign, which can be traced to the gap closing at Γ . Likewise, for fixed magnetization there is a topological transition as S_1^z changes sign.

Γ point.—The two states $|\Gamma, +\frac{1}{2}\rangle$ and $|\Gamma, -\frac{1}{2}\rangle$ have C_6 eigenvalues $e^{-i\pi/6}$ and $e^{i\pi/6}$ respectively. First order perturbation theory gives an energy correction

$$\langle \Gamma, s | J\vec{\sigma} \cdot \vec{S} | \Gamma, s \rangle = 2sJS_0^z \quad (15)$$

where $s = \pm \frac{1}{2}$. Therefore

$$\eta(\Gamma) = \begin{cases} e^{-i\pi/6} & JS_0^z < 0 \\ e^{i\pi/6} & JS_0^z > 0 \end{cases} \quad (16)$$

K point.—We start by defining the states

$$|K, \nu, s\rangle = \frac{1}{\sqrt{6}} \sum_{j=0}^5 e^{\frac{-i\pi}{6}j(2\nu+1)} \hat{C}_6^j |K, s\rangle \quad \nu = 0, 1, \dots, 5. \quad (17)$$

The six eigenspaces can be labelled by ν :

$$\hat{C}_6 |K, \nu, s\rangle = e^{\frac{i\pi}{6}(2\nu+1)} |K, \nu, s\rangle$$

The first-order effective 2×2 Hamiltonian in each eigenspace can be written $[H_\nu^{\text{eff.}}]_{ss'} = J \langle K, \nu, s | \vec{\sigma} \cdot \vec{S} | K, \nu, s' \rangle$, giving

$$H_0^{\text{eff.}} = H_3^{\text{eff.}} = J \begin{pmatrix} S_0^z + 2S_1^z & 0 \\ 0 & -S_0^z + S_1^z \end{pmatrix}, \quad (18a)$$

$$H_1^{\text{eff.}} = H_4^{\text{eff.}} = J \begin{pmatrix} S_0^z - S_1^z & 0 \\ 0 & -S_0^z + S_1^z \end{pmatrix}, \quad (18b)$$

$$H_2^{\text{eff.}} = H_5^{\text{eff.}} = J \begin{pmatrix} S_0^z - S_1^z & 0 \\ 0 & -S_0^z - 2S_1^z \end{pmatrix}. \quad (18c)$$

Let

$$\mu_K = \min[\pm J(S_0^z - S_1^z), \pm J(S_0^z + 2S_1^z)]. \quad (19)$$

It follows that

$$\theta(K) = \begin{cases} e^{i\pi/3} & \mu_K = J(S_0^z + 2S_1^z) \\ e^{-i\pi/3} & \mu_K = -J(S_0^z + 2S_1^z) \\ -1 \text{ or } e^{-i\pi/3} & \mu_K = J(S_0^z - S_1^z) \\ e^{i\pi/3} \text{ or } -1 & \mu_K = -J(S_0^z - S_1^z) \end{cases}. \quad (20)$$

The latter two cases require 2nd order perturbation theory, and thus higher Fourier harmonics, to resolve.

M point.—Define the states

$$|M, \nu, s\rangle = \frac{1}{\sqrt{6}} \sum_{j=0}^5 e^{\frac{-i\pi}{6} j(2\nu+1)} \hat{C}_6^j |M, s\rangle \quad \nu = 0, 1, \dots, 5. \quad (21)$$

Once again the six eigenspaces can be labelled by ν :

$$\hat{C}_6 |M, \nu, s\rangle = e^{\frac{i\pi}{6}(2\nu+1)} |M, \nu, s\rangle. \quad (22)$$

The first-order effective Hamiltonian in each eigenspace is given by $[H_\nu^{\text{eff.}}]_{ss'} = \langle M, \nu, s | V | M, \nu, s' \rangle$, yielding

$$H_0^{\text{eff.}} = H_2^{\text{eff.}} = H_4^{\text{eff.}} = J \begin{pmatrix} S_0^z + S_1^z & 0 \\ 0 & -S_0^z + S_1^z \end{pmatrix}, \quad (23a)$$

$$H_1^{\text{eff.}} = H_3^{\text{eff.}} = H_5^{\text{eff.}} = J \begin{pmatrix} S_0^z - S_1^z & 0 \\ 0 & -S_0^z - S_1^z \end{pmatrix}. \quad (23b)$$

Let

$$\mu_M = \min[\pm J(S_0^z + S_1^z), \pm J(S_0^z - S_1^z)]. \quad (24)$$

It follows that

$$\zeta(M) = \begin{cases} i & \mu_M = J(\pm S_0^z + S_1^z) \\ -i & \mu_M = J(\pm S_0^z - S_1^z) \end{cases}. \quad (25)$$

Berry curvature

We have produced plots of the Berry curvatures of the lowest bands in the presence of a generic SkX texture at large exchange coupling (Fig. 7c) and for the SkX and canted vortex lattice textures at weak exchange couplings (Fig. 7d).